Schumacher, D., da Rosa Braun, P.H., Wilhelm, M. et al.

Unidirectional solution-based freeze cast polymer-derived ceramics: influence of freezing conditions and templating solvent on capillary transport in isothermal wicking

Journal Article   as: peer-reviewed accepted version (Postprint)

* for better findability or for reliable citation

Recommended Citation (primary publication/Version of Record) incl. DOI:

Schumacher, D., da Rosa Braun, P.H., Wilhelm, M. et al. Unidirectional solution-based freeze cast polymer-derived ceramics: influence of freezing conditions and templating solvent on capillary transport in isothermal wicking. J Mater Sci 55, 4157–4169 (2020). https://doi.org/10.1007/s10853-019-04310-0

Take down policy
If you believe that this document or any material on this site infringes copyright, please contact publizieren@suub.uni-bremen.de with full details and we will remove access to the material.

Unidirectional solution-based freeze cast polymer-derived ceramics: influence of freezing conditions and templating solvent on capillary transport in isothermal wicking

Daniel Schumacher[1], Pedro Henrique da Rosa Braun[1], Michaela Wilhelm[1,*] , and Kurosch Rezwan[1,2]

[1] Advanced Ceramics, University of Bremen, Am Biologischen Garten 2, IW3, Bremen, Germany
[2] MAPEX—Centre for Materials and Processes, University of Bremen, Am Fallturm 1, Bremen, Germany

ABSTRACT

Porous SiOC monoliths were prepared by solution-based freeze casting of polysiloxane at constant freezing temperature or constant freezing front velocity. Dendritic and prismatic pore structures were obtained by using cyclohexane and tert-butyl alcohol as solvent, respectively. Gradients in freezing velocity lead to gradients in pore window size, whereas a constant freezing velocity (3.3–6.8 μm/s) generates homogeneous pore structures. The water permeability varies from 1.12×10^{-13} to 1.03×10^{-11} m^2 and correlates with the pore window diameter (10–59 μm) and the porosity (51–82%). In wicking tests, the gradient in pore window size is clearly reflected by a pronounced decrease in the wicking speed. Contrary, a homogeneous pore structure results in wicking curves which are closer to the prediction according to the Lucas–Washburn equation. However, this theoretical approach based on the three parameters, pore window size, porosity and permeability, is insufficient to describe complex three-dimensional pore structures. Besides the porosity, the pore morphology was found to be a major influencing factor on the wicking. The filling of secondary dendrites slows down the wicking into the dendritic structure. Fastest wicking was observed for a prismatic pore structure at low freezing front velocity (6.6 μm/s) and high porosity (78%), whereas slowest wicking occurred into the dendritic structure with high porosity (76%) and constant freezing temperature (− 20 °C). The knowledge of the relationship between structural properties and the resulting wicking behavior can address a variety of pivotal applications in chemical engineering for capillary transport.

Address correspondence to E-mail: mwilhelm@uni-bremen.de

Introduction

A wide range of industries such as power generation and storage rely on porous monolithic materials, where mass transport is a crucial property. For a large variety of applications including gas adsorption, water filtration, energy conversion/storage, catalysis and even bone tissue engineering, the control of the permeability is of great interest [1–4].

Aside from these applications, porous materials are used by the aerospace industry in, e.g., liquid acquisition devices and propellant management devices [5]. At pressures below the bubble point, a saturated porous medium prevents the penetration of gas/vapor and guarantees a gas-free delivery of, e.g., propellant to the engine. Capillary pressure is the driving force for the liquid transport [6]. Hence, pore window size and porosity highly influence the ability of a porous material to provide phase separation and liquid transportation properties. Nowadays, woven metallic screens are the standard materials in propellant management devices. The properties of non-metallic inorganic materials such as low thermal conductivity, thermal and chemical stability, corrosion resistance and low density make them an interesting alternative to metals [7].

Some studies were already conducted on the wicking of porous nonmetallic inorganic material. Wicking of various liquids including silicone oil and organic liquids into 3D-stitched C–C preforms, carbonaceous porous samples and mullite was investigated [8–10]. They found a good agreement of experimental infiltration heights with a model based on pore radii of two sizes.

In contrast to oxidic ceramics such as Al_2O_3, TiO_2 and mullite, polymer-derived ceramics can provide some benefits. Particularly, the reduced thermal conductivity is suggested being advantageous in the capillary transport of cryogenic liquids [11]. Considering the surface characteristics and its influence on the interaction between liquid and solid, polymer-derived ceramics offer the possibility to adjust properties such as hydrophilicity and specific surface area by adapting the pyrolysis temperature [12]. Besides extrusion, injection molding, additive manufacturing and reactive methods, solution-based freeze casting of preceramic polymers allows for the versatile formation of a large variety of pore window sizes, porosities and pore morphologies [13–16].

The freeze casting process which can be considered as a templating method has attracted considerable interest in recent years [17]. Although the majority of studies focus on suspension-based freeze casting (dispersed particles), solution-based freeze casting of preceramic polymers has considerable potential to create unique and promising pore structures. The segregation mechanism in solution-based freeze casting bases on thermally induced phase separation of a two-component system [16]. After phase separation during freezing, the sublimation of the solvent crystals creates the pore structure. Since the final pore structure reflects the shape of the solvent crystals, the liquid phase determines the pore morphology which can range from dendritic to prismatic, cellular or lamellar [17–19]. In order to obtain homogenous pore structures, controlling the freezing conditions is crucial. Especially the freezing front velocity highly influences the resulting pore structure, mainly the pore window size [20]. With regard to polymer-derived ceramics, SiOC structures have so far been produced with a constant freezing rate using the solution-based method [21], but systematic investigation of the orientation of the pore structures is lacking for this substance class.

Though freeze casting is able to create a large variety of pore structures and polymer-derived ceramics offer unique properties, very little is known on wicking in porous polymer-derived SiOC. In previous works of the working group, Grebenyuk et al. prepared SiOC monoliths by suspension-based freeze casting with water as dispersing medium and investigated the influence of pore window size on the wicking [22]. A comparison of experimental wicking data with predictions according to the Lucas–Washburn equation showed good agreement. Schumacher and Zimnik et al. found that predictions using the Lucas–Washburn equation differ from experimental wicking on SiOC monoliths due to a significant deviation of the pore morphology from the capillary bundle model [23]. Despite the research already conducted on porous SiOC for wicking, the influence of the freezing conditions was not yet addressed.

In this study, the influence of different freezing conditions on isothermal wicking of porous SiOC monoliths prepared by unidirectional solution-based freeze casting was investigated. Unidirectional solution-based freeze casting of preceramic polymers at constant freezing temperature or constant freezing velocity was applied for monolith preparation and

enables to study the impact of the homogeneity of the pore structure. Additionally, variations of solid loading and solvent allow for the identification of distinctions between different pore structures. Furthermore, experimental wicking data were compared with a prediction based on the Lucas–Washburn equation.

Experimental section

Materials

Porous ceramic monoliths were prepared by solution-based freeze casting. A commercial methylpolysiloxane (Silres® MK, Wacker Chemie AG, Germany) was used with (3-aminopropyl)triethoxysilane (APTES, ABCR GmbH, Germany) which served as cross-linking agent. Tert-butyl alcohol (TBA, > 99%, Thermo Fisher GmbH, Germany) and cyclohexane (CH, > 99%, Sigma-Aldrich Chemie GmbH, Germany) acted as solvents. All materials were used without further treatment or purification.

Solution-based freeze casting

The preparation of porous monolithic samples by solution-based freeze casting is shown in Fig. 1. In order to enable the reliable correlation of findings regarding the pore structure, the permeability and the wicking with the freezing conditions, all characterization was done on one sample for each composition. Heating to 50 °C in an oil bath ensured liquid state of the pure solvent TBA (T_m = 23–26 °C). In contrast, CH (T_m = 6.5 °C) was used at room temperature. Subsequent to the addition of MK and homogenization for 30 min under vigorous stirring, APTES was added at an amount of 1 mol%. After stirring was continued for 3 min, degassing at 300 mbar for 30 s removed gas bubbles created during stirring. The solution was poured into a mold, which consists of a brass bottom and a transparent polycarbonate cylinder with an inner diameter of 40 mm and a height of 90 mm. A silicone-coated polyethylenterephthalat (PET) film (Hostaphan RN 30 2SLK, Mitsubishi Polyester Film GmbH, Germany) was used as a separation layer between solution and cylinder. The use of the separation layer guaranteed easy demolding without damaging the frozen sample. The samples were frozen on a cold finger, which
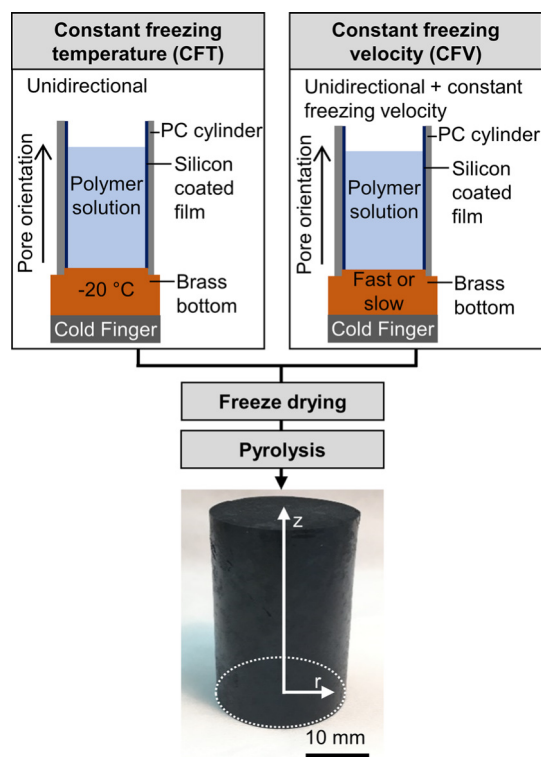

Figure 1 Process scheme of monolith preparation by solution-based freeze casting of polymeric solutions.

allows to control the temperature of the brass bottom. One end of a copper cold finger is immersed in liquid nitrogen, and the other end is equipped with a resistance heater. A thermocouple positioned at the center of the brass bottom detects the temperature at the interface between the brass bottom and sample.

Three different freezing conditions were used: constant freezing temperature (CFT) at − 20 °C and constant freezing velocity (CFV) at two different speeds (fast and slow, see Table 1). The starting conditions for CFT samples were set to 0 °C for 3 min. The data obtained by recording the freezing velocity in CFT condition were used as input to adapt the cooling ramps and empirically ensure CFV conditions. Under the assumption of a linear correlation between the cooling rate and the freezing front velocity, the local deviation of the freezing front velocity in CFT conditions from the constant freezing front velocity was taken as a parameter for changing the cooling ramps. The starting conditions for CFT samples were set to 0 °C for 3 min. After complete freezing, the mold was transferred to a freezer at a temperature of − 20 °C for 72 h to enable sufficient cross-linking. Subsequently, the solvent was

Table 1 Denotation, composition, freezing conditions and experimental freezing front velocity

Denotation	Solvent	Solid loading wt%	Freezing condition	Experimental freezing front velocity μm/s
CH20-20	Cyclohexane	20	CFT[a] − 20 °C	–
CH40-20	Cyclohexane	40	CFT[a] − 20 °C	–
TBA20-20	Tert-butyl alcohol	20	CFT[a] − 20 °C	–
TBA40-20	Tert-butyl alcohol	40	CFT[a] − 20 °C	–
CH20fast	Cyclohexane	20	CFV[b] fast	6.8
CH40fast	Cyclohexane	40	CFV[b] fast	6.6
TBA20fast	Tert-butyl alcohol	20	CFV[b] fast	6.6
TBA40fast	Tert-butyl alcohol	40	CFV[b] fast	6.8
CH20slow	Cyclohexane	20	CFV[b] slow	4.6
CH40slow	Cyclohexane	40	CFV[b] slow	4.2
TBA20slow	Tert-butyl alcohol	20	CFV[b] slow	4.6
TBA40slow	Tert-butyl alcohol	40	CFV[b] slow	3.3

[a]*CFT* constant freezing temperature

[b]*CFV* constant freezing velocity

sublimated in a freeze dryer for 72 h at a shelf temperature of − 20 °C and a pressure of 1000 μbar. Lastly, the samples were pyrolyzed at 1000 °C under flowing nitrogen with a heating rate of 2 K/min and a dwelling time of 4 h. Before characterization, 2 mm of the bottom end was removed to ensure an open access to the pore structure and a flat cross section. Additionally, cutting all samples to a total height of 25 mm guarantees comparability in wicking experiments. After the wicking tests, the monoliths were cut horizontally to obtain samples for the height-dependent investigation of pore window size, porosity and permeability. Three positions were taken into account: bottom, middle and top. The middle positions correspond to a height of 12.5 mm, and all samples were taken from identical positions.

The samples were given the nomenclature: [solvent] [solid loading in wt%] [freezing condition]. Whereby, the polymer and the cross-linking agent counted as solid fraction. Table 1 gives an overview of all samples and their compositions.

Characterization

The freezing front axial advance of one sample for each composition was recorded during the freezing process by a CCD-camera in order to evaluate the freezing front velocity. The pore structure at the positions bottom, middle and top was investigated using a scanning electron microscope (SEM, Camscan Series2, Obducat CamScan Ltd.) with samples mounted on carbon tape. Before acquisition, specimens were sputtered with gold (K550, Emitech, Judges Scientific Plc., UK). Pore window diameter distribution and open porosity ϕ at the positions bottom, middle and top were obtained by mercury intrusion porosimetry (Pascal 140/440, POROTEC GmbH, Germany).

The permeability $K = K_{Darcy}$ at the positions bottom and top was evaluated in axial z-direction according to Darcy's law in constant head measurements on cylindrical samples with a diameter of $D_{Darcy} = 10$ mm and a height of $H_{Darcy} = (5–9)$ mm. Suitable cylindrical samples were cut from the center of the corresponding cross sections. Bypass flow was minimized by using a compressible silicone sample holder. The mass of the permeated water $m_{w,Darcy}$ at a pressure difference Δp_{Darcy} of 10 kPa and a time t of 300 s was recorded. With the dynamic viscosity of water at 20 °C $\mu_w = 1.00$ mPas and the density of water at 20 °C $\rho_w = 998$ kg/m^3, the permeability $K = K_{Darcy}$ was calculated according to Eq. (1). Soaking the specimens with water before the measurement should reduce deviations due to intake losses. Each sample was tested minimum five times, and the average was calculated. In order to obtain reliable results, the validity assumptions of the Darcy equation have been verified. Since calculated Reynolds numbers range from 2 to 1450, the presence laminar flow regime is indicated. Further

requirements such as no reaction of the fluid with the sample, incompressible fluid, single phase flow and continuous and steady flow can be considered as fulfilled. Thus, the applicability of the Darcy equation is ensured.

$$K = K_{\text{Darcy}} = \frac{\mu_{\text{W}} H_{\text{Darcy}}}{\Delta p_{\text{Darcy}}} \frac{m_{\text{W,Darcy}}}{\rho_{\text{W}} \frac{\pi}{4} D_{\text{Darcy}}^2 t_{\text{Darcy}}}. \tag{1}$$

The Washburn sorption method was used to investigate wicking into porous media when in contact with a liquid. Figure 2 shows a schematic drawing of the wicking device.

The mass increase in the sample caused by imbibing liquid was recorded by a balance (LA310S, Sartorius AG, Germany) with a precision of ± 0.0001 g and a sample rate of 20 Hz. The scale was mounted on a height-adjustable platform which allows for bringing the sample in contact with the liquid. The specimen was attached to a sample holder and connected by a metallic wire with the balance. The surrounding container has a diameter of 0.095 m, and its lid has a small hole allowing for a frictionless movement of the sample. Hydrofluoroether (HFE-7500, 3 M$^{\text{TM}}$ Novec$^{\text{TM}}$) was used as test liquid, because it shows excellent wetting properties for a wide range of materials. Hence, a contact angle of $\theta = 0°$ was assumed [7]. Once the sample had contact with the liquid, the immersion process was stopped. After wicking to complete saturation indicated by a constant mass signal m_{sat}, the monolith was lifted approx. 5 mm to lose contact with the liquid. All wicking tests were performed under room temperature and at ambient pressure. The geometry of the device leads to the assumption of negligible decreasing liquid level, whereas buoyancy and the Wilhelmy effect result in the necessity of raw data corrections. The Wilhelmy effect describes the mass change due to surface tension. Following previous studies, th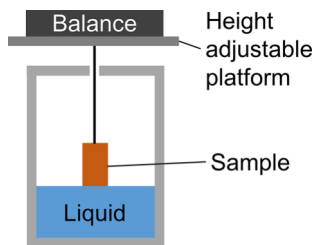e weight of the completely saturated, but partially submerged sample was subtracted from the weight of the completely saturated sample [22, 24].

Besides the experimental approach, wicking can be evaluated by calculating the liquid transport. The capillary bundle model was used for the theoretical prediction of the wicking. The capillary pressure, which results from the curvature of the surface, is the driving force for the wicking. Viscous forces and hydrostatic pressure balance the capillary pressure [22, 23, 25–27]:

$$\frac{m^2}{t} = \frac{4\sigma_{\text{l}} \cos\theta \rho_{\text{l}}^2 A^2 \phi}{\mu_{\text{l}}} \frac{K}{R_{\text{s}}}. \tag{2}$$

This equation gives the imbibed mass m per time t and is called the Lucas–Washburn equation with gravity effects for porous media with σ_{l} being the surface tension of the liquid, θ the contact angle, R_{s} the static radius, ϕ the open porosity, μ_{l} the dynamic viscosity of the liquid, K the permeability, ρ_{l} the density of the liquid, g the gravitational acceleration and A the cross section of the sample. According to the product sheet of the supplier, the surface tension σ_{l}, the dynamic viscosity μ_{l} and the density ρ_{l} of HFE-7500 are 16.2×10^{-3} N m^{-1}, 1.24×10^{-3} Pa s and 1614 kg m^{-3}, respectively [28]. As already mentioned, the contact angle θ can be assumed to be 0°. Wicking can be predicted with the knowledge of the macroscopic properties describing the porous structure such as the static radius R_{s}, the open porosity ϕ and the permeability K. The static radius R_{s} describes an equivalent capillary pore radius and can be calculated from the equilibrium between capillary pressure and hydrostatic pressure. Due to the limited height of the samples in this study, the equilibrium was not reached and the static radius R_{s} could not be calculated. Instead, the mean pore window radius R_{merc} determined by mercury intrusion porosimetry was used as static radius.

Results and discussion

Freezing process

To evaluate the freezing front velocity, the axial advance of the freezing front was monitored during freezing as shown in Fig. 3.

Constant freezing temperature conditions (CFT) are characterized by a clear decrease in freezing front velocity with time. The thermal resistance increases

Figure 2 Schematic drawing of the device for isothermal wicking at room temperature.

Figure 3 Position of freezing front during freeze casting in dependence on solvent, solid loading and freezing conditions; the theoretical constant freezing front velocity is symbolized by the dashed lines.
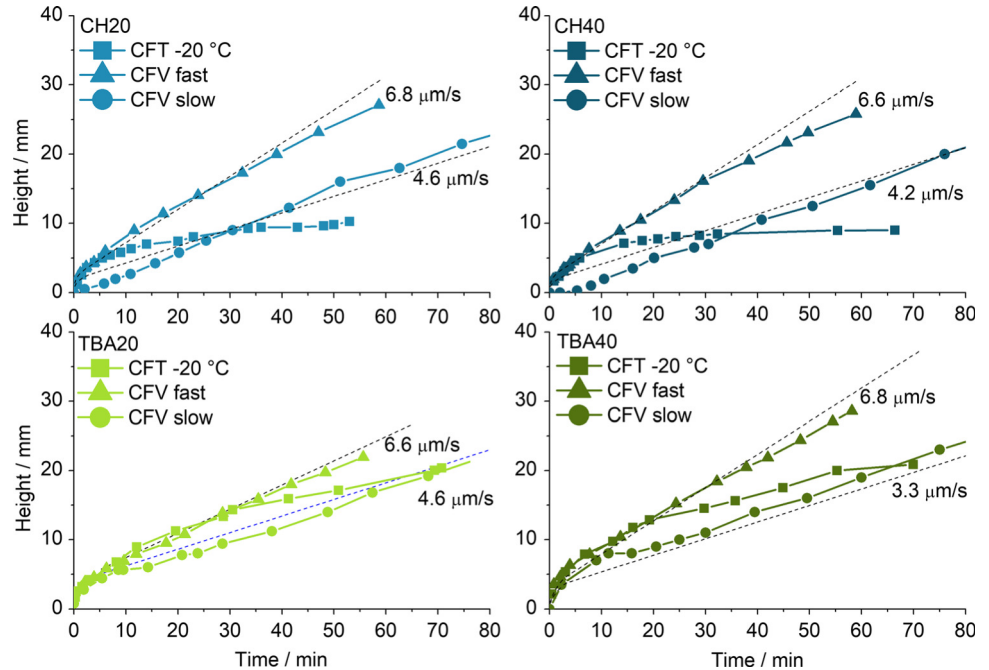
with progressing freezing front leading to a decrease in the thermal gradient at the freezing front. Since the freezing front velocity is mainly influenced by the thermal gradient, it decreases with time [29]. While the solid loading (20 or 40 wt%) does not affect the freezing front velocity at CFT conditions (rectangles in Fig. 3), the solvent clearly has an impact. At the same conditions, the freezing front reaches only half of the height in cyclohexane samples compared to samples with tert-butyl alcohol. One reason is the higher temperature difference between freezing temperature and melting point for TBA which translates into a higher undercooling. Though the thermal conductivity of the solid solvent is supposed to be an influencing factor, no estimation is possible due to the lack of data for TBA. The thermal conductivity of CH at $-25\,°C$ was reported to be $0.14\ W\ m^{-1}\ K^{-1}$ [30]. In the liquid state, CH and TBA exhibit a similar thermal conductivity with values of $0.117\ W\ m^{-1}\ K^{-1}$ (27.68 °C) and $0.1076\ W\ m^{-1}\ K^{-1}$ (27.8 °C), respectively [31, 32].

When adapting the temperature program, two different constant freezing front velocities were achieved indicated by an almost constant slope in Fig. 3. The theoretical velocity is symbolized by the dashed lines. The empirical approach which uses the data of CFT conditions to obtain CFV conditions proofs to be efficient for the investigated parameters. Due to the initial freezing stage at 0 °C for 3 min, the

theoretical velocity as well as the experimental data starts with a nonlinear section. The realized freezing front velocities were influenced by the composition and differ from 3.3 to 6.8 μm/s. Constant freezing front velocities over the complete height of the sample are easier to achieve for slow freezing front velocities. Especially at low freezing front velocities, the freezing front velocity during the initial freezing stage deviates from the average velocity. Depending on the solvent, the freezing front velocity deviates to higher or lower velocities. Due to different melting points of TBA (T_m = 23–26 °C) and CH (T_m = 6.5 °C), the thermal gradient at initial freezing (0 °C) is higher for TBA compared to CH, which is why TBA20slow and TBA40slow show faster initial freezing. In contrast, CH20slow and CH40slow froze significant slower at the initial stage. Furthermore, precise evaluation of the position of the freezing front is difficult resulting in scattered data. The formation of ice on the outer surface of the mold and the meniscus-shaped solidification front which is generated by the heat transfer from the bottom through the cylindrical mold to the solidification front are main difficulties.

Pore structure

The influence of the freezing front velocity on the pore structure was height-dependently investigated

at three positions: bottom, middle and top. Figure 4 shows representative cross-sectional SEM images of the pore structure parallel to the freezing direction and schematical representations of one dendrite along the complete sample height.

Due to the unidirectional freezing, the pore structure is orientated from bottom to top. The characteristic dendritic and prismatic pore morphology is present for cyclohexane and tert-butyl alcohol, respectively [16].

Investigations by mercury intrusion porosimetry enable a detailed characterization of the pore structure. The mean pore window diameters (a) and open porosities (b) are shown in Fig. 5.

The porosity is almost constant within one sample. The solid loading is the main influencing factor on porosity with higher porosity at lower solid loading as it is described in literature [33]. The porosity ranges from 51 to 82%. Regarding the pore window size, lower solid loading results in slightly larger pore window diameters. In general, the pore window size distribution is mainly monomodal as it can be seen exemplarily in Figure S2. In addition to the solid loading, the solvent influences the pore window size with the prismatic pore morphology (TBA) leading to larger pore window sizes compared to the dendritic (CH) one. All samples frozen at CFT conditions exhibit an increasing pore window size from bottom to top of factors between 1.2 and 3.5. This is in accordance with SEM images since Fig. 4 shows the same trend.

Comparison with the recorded freezing front velocity indicates a strong relation between freezing front velocity and pore window size. Hence, a gradient in freezing front velocity leads to a gradient in pore window size with slow freezing resulting in large pores. This correlation was also reported in the literature for suspension-based freeze casting using water as liquid phase [20]. In contrast, a constant freezing front velocity generates a homogeneous pore window size as it can be observed for most of the samples frozen at CFV conditions. Significant deviations from constant pore window sizes in CFV conditions for example in TBA40slow and CH20slow are caused by locally different freezing front velocities. In Fig. 3, faster and slower freezing than the average freezing front velocity during the course of freezing are obvious for CH20slow and TBA40fast, respectively. By adapting the freezing front velocity, the generation of samples with different homogenous pore window sizes is possible. This is valid for both solvents. Decreasing the freezing front velocity from CFV slow to CFV fast conditions results in an increase in the pore window diameter by 16%, 29%, 14% and 67% for CH20, CH40, TBA20 and TBA40, respectively. Hence, samples with higher solid loading are more sensitive to variations in freezing front velocity and allow for a larger range of achievable pore window sizes. At large pore window sizes, the thermodynamics of crystal growth are assumed to slow down the increase in pore window size with decreasing freezing front. While small pore window sizes at low solid loading are difficult to achieve due

Figure 4 Exemplary cross-sectional SEM images of the pore structure for bottom, middle and top position in dependence on solvent, solid loading and freezing conditions; scale bar: 50 µm.
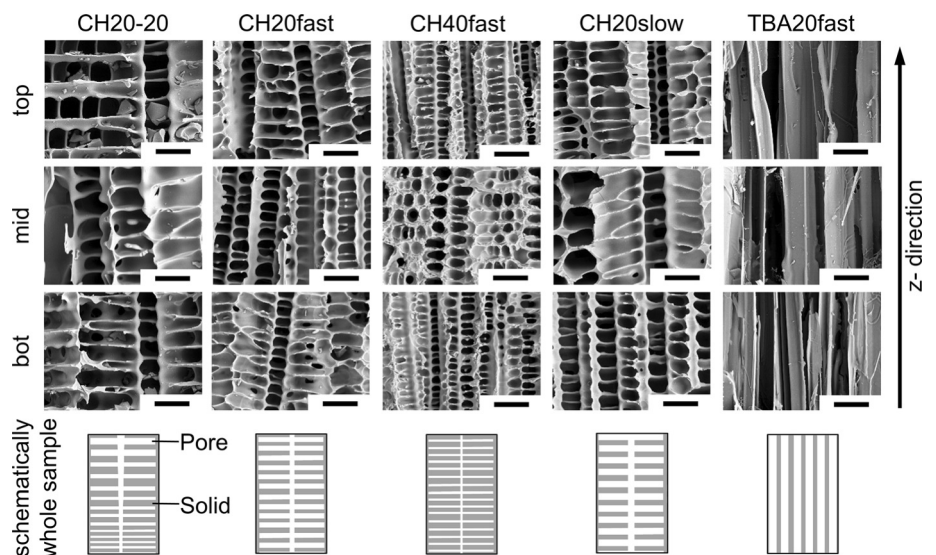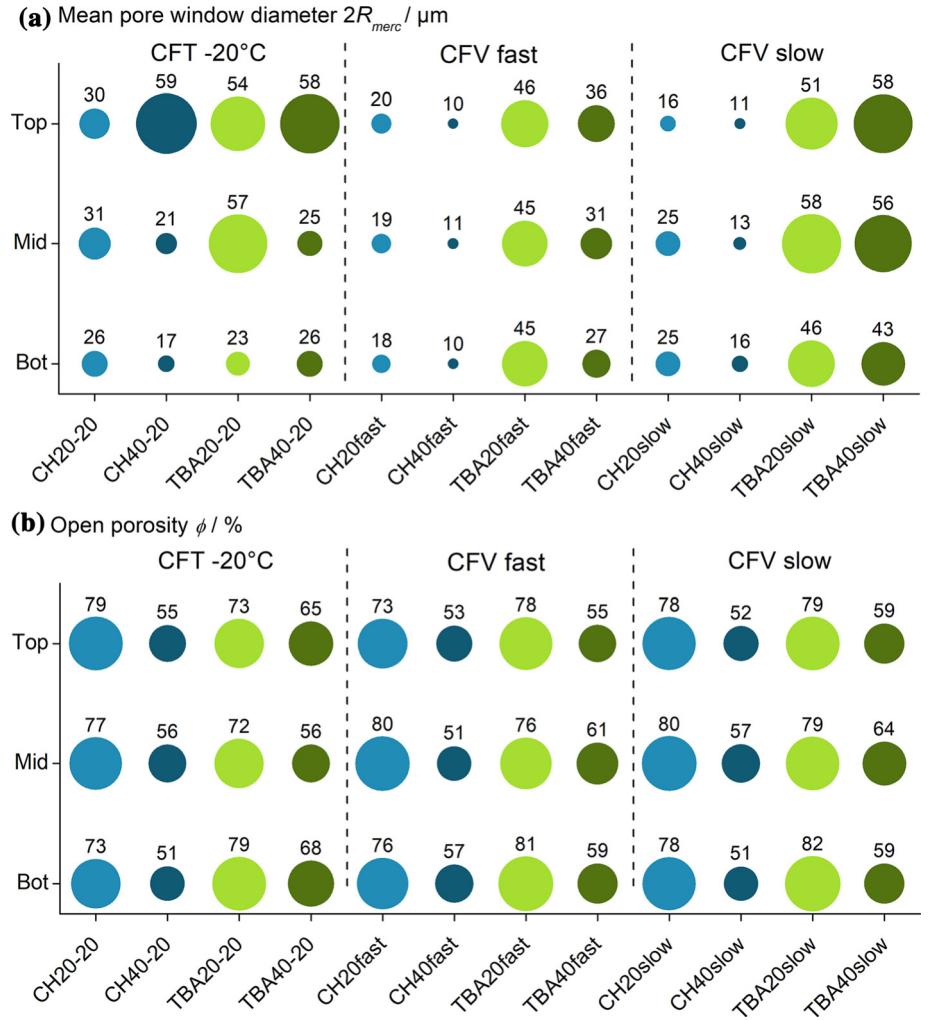
Figure 5 Mean pore window diameter (**a**) and open porosity (**b**) in dependence on the position obtained by mercury intrusion.

(**a**) Mean pore window diameter $2R_{merc}$ / µm

(**b**) Open porosity ϕ / %

Permeability

to the dependence of the pore window size from the solid loading, decreasing the freezing front velocity to obtain larger pores at high solid loading is easily possible. The combination of the different influencing factors on the pore window size such as solid loading, solvent and freezing front velocity with CFV freezing conditions enables the preparation of samples with a homogenous pore structure. The pore window size can be adjusted in the range of 10 to 69 µm. Besides creating a homogenous pore structure, the knowledge of the relation between freezing front velocity and resulting pore window size also allows for the generation of defined gradients in pore window size by adapting the freezing front velocity.

The permeability K of bottom and top positions and the ratio between top and bottom position are shown in Fig. 6.

Permeabilities in the range of 1.12×10^{-13} to 1.03×10^{-11} m^2 were measured. In general, decreasing permeability with decreasing porosity obtained by higher solid loading is observed for all freezing conditions and both solvents [34]. All samples with cyclohexane as liquid exhibit lower permeability compared to samples prepared at the same conditions with tert-butyl alcohol. This can be mainly attributed to the smaller pore window sizes of CH samples compared to TBA samples. The relation between permeability K and pore structure is usually modeled based on [35]:

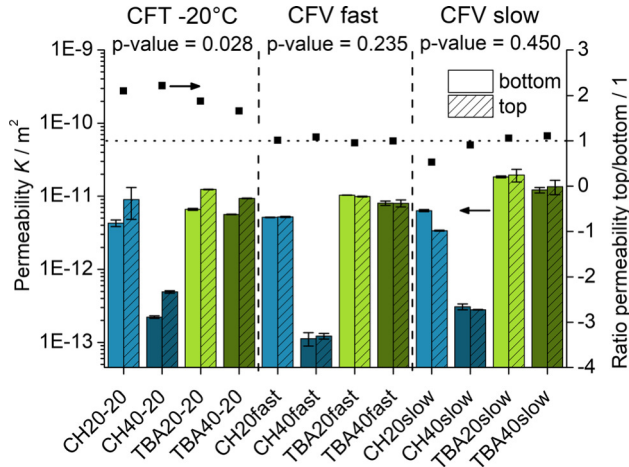$$K = c_{\text{geo}}\phi R^2, \tag{3}$$

Figure 6 Permeability of top and bottom position and ratio between permeability of top and bottom position depending on solvent, solid loading and freezing condition.

where R is the pore radius, ϕ is the porosity, and c_{geo} is a geometric factor that describes the shape, connectivity and aspect ratio of the pores. Equation (3) indicates that the permeability is very sensitive to the pore radius. The trend of pore window sizes obtained by mercury intrusion is in good accordance with the resulting permeability. Furthermore, for CFT conditions a gradient in pore window sizes is present which is reflected by higher permeability of all CFT samples at the top position. Hence, the ratio between the permeability of top and bottom positions is larger than one. In contrast, CFV conditions with the homogenous pore window sizes result in ratios close to one. Only CH20slow shows a non-constant permeability with a significant lower permeability at the top compared to the bottom position. Statistical analysis on the significance of the differences between top and bottom positions revealed p values of 0.028, 0.235 and 0.450 for CFT, CFV fast and CFV slow conditions, respectively. As the p value for CFV fast and CFV slow conditions is larger than the significance level of 0.05, the difference in permeability can be considered to be statistically non-significant for CFV fast and CFV slow conditions. In contrast, CFT exhibits statistically significant differences between top and bottom position (p value < 0.05).

When comparing this finding with the pore window size, it becomes clear that the change in permeability is caused by differing pore window sizes. In contrast, the decrease in pore window size for

CH40slow from bottom to top is assumed to be too low to significantly influence the experimentally obtained permeability. While TBA20 shows the highest permeability for all freezing conditions, CH40 exhibits the lowest permeability. Again, this can be clearly attributed to the different pore window sizes. For the same conditions, TBA generates larger pores compared to CH as can be seen in Fig. 5. The geometric factor c_{geo} was calculated according to Eq. (3). 0.0611 ± 0.0160, 0.0086 ± 0.0013, 0.0358 ± 0.0135 and 0.0427 ± 0.0176 were obtained for CH20, CH40, TBA20 and TBA40, respectively. For samples prepared with TBA, the change in solid loading has no significant influence on the c_{geo} value. This indicates no influence of the solid loading on structural parameters such as pore shape, pore connectivity and aspect ratio. In contrast, the c_{geo} value of samples with a dendritic pore structure (CH) depends on the solid loading. Hence, structural parameters describing the pore structures change with solid loading for a dendritic pore morphology. Lower solid loading accompanied with a higher porosity and a larger pore window size induces a high c_{geo} value in CH samples. This suggests that describing and predicting the permeability of the dendritic pore structure is more complex compared to the prismatic pore structure. In the literature, permeability, porosity and pore window size results which lead to a c_{geo} value of 0.0508 were reported for a dendritic pore structure obtained by a similar process [36]. This c_{geo} value is close to the one of CH20 and indicates comparable pore structures. Investigations on c_{geo} values of granular material such as sandstone and volcanic rock reveals values of 0.012 and 0.0022, respectively [35]. The deviation of the c_{geo} values for freeze cast structures from c_{geo} values reported for granular material can be explained by considerable differences in the pore morphology. Only the c_{geo} value of CH40 is in the range of granular material.

It has to be mentioned that especially the permeability measurement of TBA20 is prone to bypass flow due to the low mechanical stability of the sample and potential crack formation when mounting the sample to the sample holder. As a consequence, the permeability of TBA20 samples is potentially overestimated.

Wicking and theoretical prediction of wicking

The results of isothermal wicking experiments grouped by composition are shown in Fig. 7.

While at short times the viscosity of the liquid is most influencing, longer times are increasingly dominated by the influence of the gravity [37]. Samples frozen at higher velocity reach the saturation mass faster for all compositions. A higher freezing front velocity is connected to a smaller pore window size which results in faster wicking according to Eq. (2). According to Eq. (3), a smaller pore window size is also related to a lower permeability which decreases the wicking speed. However, the wicking results indicate that this decrease in permeability is not sufficient to compensate the increase in wicking speed caused by a small pore window size. The smaller the pore window size the higher the capillary force which is the driving force for wicking. At short times, wicking curves of samples prepared at CFT conditions follow the behavior of fast frozen CFV samples. During the course of the experiment, the wicking speed significantly slows down to values which are smaller than samples frozen at slow CFV conditions. Besides the influence of the gravity, this can be mainly attributed to the gradient in pore window size along the axial height of the sample. Consequently, a gradient in pore window size creates

a gradient in the driving force which changes the wicking speed additionally to the influence of gravity.

The influence of the porosity can be seen in Fig. 8 which shows the wicking curves in dependence on solvent and solid loading grouped by freezing conditions. For all freezing conditions of TBA samples, higher porosity and larger pore window size caused by lower solid loading result in faster wicking. According to Eq. (3), increasing porosity and pore window size translate into increasing permeability which can be attributed to be the main reason for faster wicking of samples with lower solid loading. For CH samples, this trend is not consistent. The influence of the pore morphology becomes obvious when comparing CH20 samples with TBA samples. Although all three CH20 samples exhibit similar permeability, CH20-20 and CH20slow wick considerably slower than CH20fast. The reasons for this behavior are unclear at the moment. The wicking into the dendritic pore structure is generally slower than into the prismatic structure. Secondary dendrites which are perpendicular to primary ones need to be filled during wicking by flow through primary dendrites. Hence, in the dendritic pore morphology a higher pore volume has to be filled through smaller pores compared to the prismatic structure of the TBA samples. With a time of 10.9 s until saturation, TBA20fast exhibits the fastest wicking of all

Figure 7 Mass divided by saturation mass in dependence on solvent and solid loading for all freezing conditions.
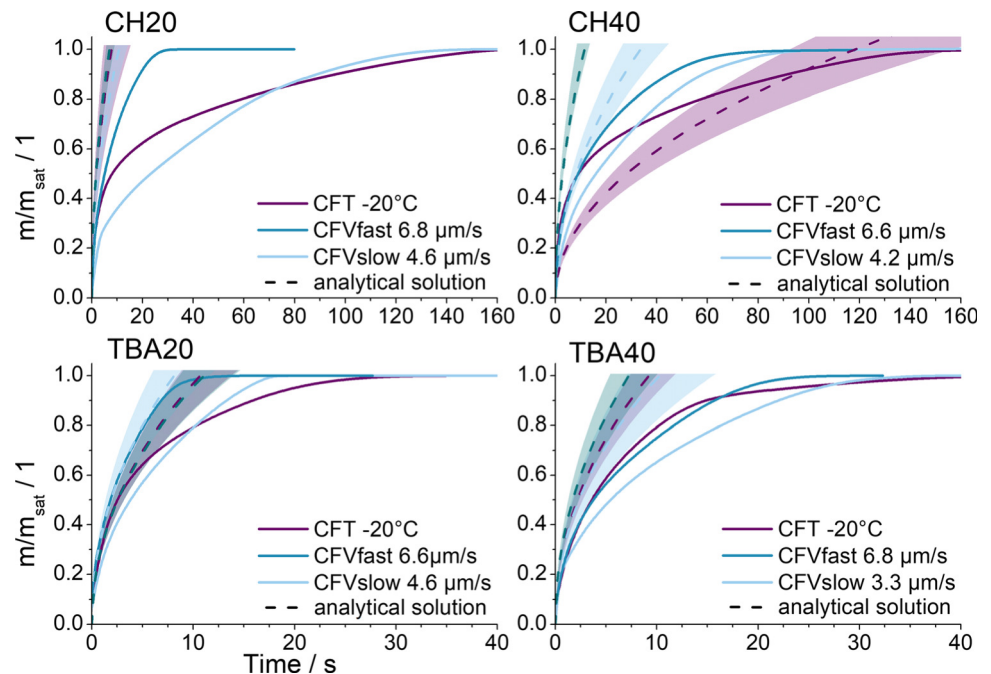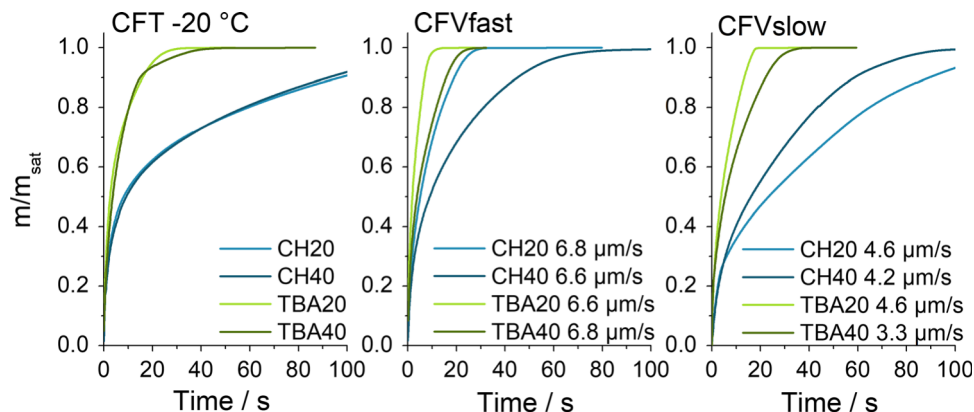
Figure 8 Wicking curves grouped by freezing condition in dependence on solvents and solid loading.

investigated samples, whereas CH20-20 shows the slowest wicking with 151.7 s. In between those limits, the wicking speed can be changed. Furthermore, a gradient in the driving force can be generated by a gradient of the pore window size. The knowledge of the factors influencing the wicking and the possibility to easily adapt the pore structure make it possible to precisely tailor materials for several applications in capillary transport.

Theoretical wicking curves were calculated according to the Lucas–Washburn equation as can be seen in Fig. 7. The experimentally observed trend in wicking speed CFVfast > CFVslow is reflected in the analytical solution for all samples besides TBA20. The term ($\Phi K/R_s$) which describes the pore structure is significantly higher for TBA20slow compared to the other samples. Also, the ratio between permeability and static radius (K/R_s) is considerable larger for TBA20CFVslow. The potential overestimation of the permeability of TBA20 samples might be a reason for the high ratio. Concerning the influence of the porosity on wicking, the theoretical considerations confirm the experimental finding of faster wicking at higher porosity for both solvents. Except for TBA20, the analytical solution shows a significant deviation from the experiment for the following reason. The Lucas–Washburn equation assumes a bundle of aligned capillary tubes of the same radii. This assumption holds only for TBA20 which has a prismatic pore structure and an open porosity of approx. 75%. Decreasing the porosity to approx. 60% or even changing to a dendritic pore structure leads to a pronounced overestimation of the wicking speed by the analytical solution. Additionally, the analytical solution is not able to reflect gradients in the pore window size as they are present in the CFT samples. As a consequence, the prediction of wicking into

complex pore structures by the Lucas–Washburn equation is only possible for pore structures which exhibit a very specific set of properties.

A previous study by the authors investigating the wicking of non-unidirectional frozen samples revealed a peculiar wicking behavior for the dendritic pore structure with a pronounced linear section in the wicking curve [23]. The authors suggested that limited interconnectivity between aligned pore areas is a potential explanation. In the present work, samples were frozen unidirectional and no linear section in the wicking tests was observed. Unidirectional freezing ideally provides a fully aligned pore structure with dendrites or prismatic pore channels running from bottom to top without any interruption. Hence, the absence of a linear section in wicking curves of the dendritic structures in the present study supports the assumption of limited interconnectivity causing the reported linear wicking behavior [23].

Conclusion

In this study, porous SiOC monoliths were prepared by solution-based freeze casting and the influence of different freezing conditions on the pore structure and on isothermal wicking was investigated. Constant freezing temperature results in a gradient of the pore window size, whereas constant freezing velocities between 6.8 µm/s and 3.3 µm/s lead to homogeneous pore structures. This was proved by characterizing the pore structure at three different positions of the monolith. The homogeneity holds for dendritic and prismatic pore structures and different porosities. In dependence on the solid loading, the solvent and the freezing front velocity, the pore window size varies between 10 and 59 µm.

Maintaining solvent and solid loading constant, a higher freezing front velocity reduces the pore window size. The permeability varies in the range of 1.12×10^{-13} to 1.03×10^{-11} m^2 and is in good agreement with trends found for the pore window diameter and the porosity. Fastest wicking was observed for a prismatic pore structure at low freezing front velocity and high porosity, whereas slowest wicking occurred into the dendritic structure with high porosity and constant freezing temperature. The gradient of pore window size in samples prepared at constant freezing temperature is clearly reflected by a pronounced decrease in the wicking speed. In contrast, preparation at constant freezing front velocity results in wicking curves which have a shape closer to the prediction according to the Lucas–Washburn equation. The wicking of only the prismatic structure with a porosity of approx. 75% can be sufficiently described by the Lucas–Washburn equation. Contrary, the simplification of reducing complex three-dimensional pore structures to the three parameters pore window size, porosity and permeability is not applicable for predicting the wicking behavior of the other investigated structures. The knowledge of the relationship between structural properties and the resulting wicking behavior combined with the flexibility of the solution-based freeze casting process enables to tailor porous media. A wide range of applications in capillary transport can be addressed by this powerful combination.

Acknowledgements

Electronic supplementary material: The online version of this article (https://doi.org/10.1007/s10853-019-04310-0) contains supplementary material, which is available to authorized users.

References

[1] Ahmad NA, Leo CP, Ahmad AL, Ramli WKW (2014) Membranes with great hydrophobicity: a review on preparation and characterization. Sep Purif Rev 44:109–134

[2] Zhu X, Li S, Shi Y, Cai N (2019) Recent advances in elevated-temperature pressure swing adsorption for carbon capture and hydrogen production. Prog Energy Combust Sci 75:100784

[3] Bhatia SK, Bhatia RK, Jeon J-M, Kumar G, Yang Y-H (2019) Carbon dioxide capture and bioenergy production using biological system—a review. Renew Sust Energy Rev 110:143–158

[4] Baino F, Fiume E, Barberi J et al (2019) Processing methods for making porous bioactive glass-based scaffolds—a state-of-the-art review. Int J Appl Ceram Technol 16:1762–1769

[5] Hartwig J (2016) Liquid acquisition devices for advanced in-space cryogenic propulsion systems. Elsevier Inc, Amsterdam

[6] Masoodi R, Pillai KM (2013) Wicking in porous materials. CRC Press, Cambridge

[7] Fries N, Odic K, Conrath M, Dreyer M (2008) The effect of evaporation on the wicking of liquids into a metallic weave. J Colloid Interface Sci 321:118

[8] Einset EO (1996) Capillary infiltration rates into porous media with applications to silcomp processing. J Am Ceram Soc 79:333–338

[9] Kumar S, Kumar A, Devi R, Shukla A, Gupta AK (2009) Capillary infiltration studies of liquids into 3D-stitched C-C preforms. Part B: kinetics of silicon infiltration. J Eur Ceram Soc 29:2651–2657

[10] Okada K, Uchiyama S, Isobe T, Kameshima Y, Nakajima A, Kurata T (2009) Capillary rise properties of porous mullite ceramics prepared by an extrusion method using organic fibers as the pore former. J Eur Ceram Soc 29:2491

[11] Zhang H, Fidelis CL, Wilhelm M, Xie Z, Rezwan K (2017) Macro/mesoporous SiOC ceramics of anisotropic structure for cryogenic engineering. Mater Des 134:207

[12] Colombo P, Mera G, Riedel R, Sorarù GD (2010) Polymer-derived ceramics: 40 years of research and innovation in advanced ceramics. J Am Ceram Soc 93:1805–1837

[13] Vakifahmetoglu C, Zeydanli D, Colombo P (2016) Porous polymer derived ceramics. Mater Sci Eng R 106:1–30

[14] Colombo P (2008) Engineering porosity in polymer-derived ceramics. J Eur Ceram Soc 28:1389

[15] Yoon B-H, Park C-S, Kim H-E, Koh Y-H (2007) In situ synthesis of porous silicon carbide (SiC) ceramics decorated with SiC nanowires. J Am Ceram Soc 90:3759–3766

[16] Naviroj M, Miller SM, Colombo P, Faber KT (2015) Directionally aligned macroporous SiOC via freeze casting of preceramic polymers. J Eur Ceram Soc 35:2225–2232

[17] Scotti KL, Dunand DC (2018) Freeze casting—a review of processing, microstructure and properties via the open data repository FreezeCasting.net. Prog Mater Sci 94:243–305

[18] Tang Y, Qiu S, Wu C, Miao Q, Zhao K (2016) Freeze cast fabrication of porous ceramics using tert-butyl alcohol–water crystals as template. J Eur Ceram Soc 36:1513–1518

[19] Miller SM, Xiao X, Faber KT (2015) Freeze-cast alumina pore networks: effects of freezing conditions and dispersion medium. J Eur Ceram Soc 35:3595–3605

[20] Deville S, Saiz E, Tomsia AP (2007) Ice-templated porous alumina structures. Acta Mater 55:1965–1974

[21] Naviroj M, Voorhees PW, Faber KT (2017) Suspension- and solution-based freeze casting for porous ceramics. J Mater Res 32:3372–3382

[22] Grebenyuk Y, Zhang HX, Wilhelm M, Rezwan K, Dreyer ME (2017) Wicking into porous polymer-derived ceramic monoliths fabricated by freeze-casting. J Eur Ceram Soc 37:1993–2000

[23] Schumacher D, Zimnik D, Wilhelm M, Dreyer M, Rezwan K (in press) Solution based freeze cast polymer derived ceramics for isothermal wicking—relationship between pore structure and imbibition. Sci Technol Adv Mater

[24] Grebenyuk Y, Dreyer ME (2016) Wicking of liquid nitrogen into superheated porous structures. Cryogenics 78:27–39

[25] Washburn EW (1921) The dynamics of capillary flow. Phys Rev 17:273–283

[26] Masoodi R, Pillai KM, Varanasi PP (2007) Darcy's law-based models for liquid absorption in polymer wicks. AlChE J. 53:2769–2782

[27] Masoodi R, Pillai KM, Varanasi PP (2008) In: Asme (ed) Proceedings of FEDSM2008 2008 ASME Fluids Engineering Conference

[28] M Deutschland GmbH, Product Information 3 M Novec 7500 Engineered Fluid (2019)

[29] Wegst UG, Schecter M, Donius AE, Hunger PM (2010) Biomaterials by freeze casting. Philos Trans A Math Phys Eng Sci 368:2099–2121

[30] Andersson P (1978) Thermal conductivity and heat capacity of cyclohexane under pressure. J Phys Chem Solids 39:65–68

[31] Watanabe H, Kato H (2004) Thermal conductivity and thermal diffusivity of twenty-nine liquids: alkenes, cyclic (alkanes, alkenes, alkadienes, aromatics), and deuterated hydrocarbons. J Chem Eng Data 49:809–825

[32] Cameo Chemicals Database United States Government (1999)

[33] Deville S (2008) Freeze-casting of porous ceramics: a review of current achievements and issues. Adv Eng Mater 10:155–169

[34] Hommel J, Coltman E, Class H (2018) Porosity-permeability relations for evolving pore space: a review with a focus on (bio-)geochemically altered porous media. Transp Porous Med 124:589–629

[35] Nishiyama N, Yokoyama T (2017) Permeability of porous media: role of the critical pore size. J Geophys Res Solid Earth 122:6955–6971

[36] Mikl G, Obmann R, Schörpf S, Liska R, Konegger T (2019) Pore morphology tailoring in polymer-derived ceramics generated through photopolymerization-assisted solidification templating. Adv Eng Mater 21:1900052

[37] Fries N, Dreyer M (2008) An analytic solution of capillary rise restrained by gravity. J Colloid Interface Sci 320:259–263